

Mie scattering due to tissue structures in the terahertz regime: Experimental and Monte Carlo verification using diffused polarimetric imaging in highly attenuating tissue phantoms

Erica Heller^a, Kuangyi Xu^a, Zachery Harris^a, M. Hassan Arbab^{a,*}

^aStony Brook University, Department of Biomedical Engineering, 100 Nicolls Road, Stony Brook, NY, United States, 11794

Abstract.

Significance: Changes in the structure of tissue occur in many disease processes, such as the boundaries of cancerous tumors and burn injuries. Spectroscopic and polarimetric alterations of terahertz light caused by Mie scattering patterns has the potential to be a diagnostic marker.

Aim: We present an analysis of Monte Carlo simulation of Mie scattering of polarized terahertz light from cancerous tumor budding, compare the simulation to experimental results obtained in phantom models, and present an analysis of a polarization-sensitive terahertz scan of an ex vivo porcine burn injury.

Approach: Using a Monte Carlo simulation, we modeled the changes in diffuse intensity and degree of polarization of broadband off-specular terahertz light due to scattering particles in highly attenuating tissue. We extracted the Mueller matrix of the tissue using this model and analyzed its Lu-Chipman product decomposition matrices. We compared this model to experimental data from four phantoms consisting of polypropylene particles of varying sizes embedded in gelatin. Finally, we induced a full-thickness burn injury in ex vivo porcine skin samples and compared experimental data from burned and healthy regions of the tissue.

Results: Simulation revealed contrast in the Stokes vectors and Mueller Matrix elements for varying scattering particle sizes. Experimental phantom results showed contrast between different sizes of scattering particles in degree of polarization and diffuse intensity in agreement with Monte Carlo simulation results. Finally, we demonstrated a similar diffused imaging signal contrast between burned and healthy regions of ex vivo porcine skin.

Conclusion: Polarimetric terahertz imaging has the potential to detect structural changes due to biological disease processes.

Keywords: Terahertz time-domain spectroscopy and polarimetry, THz-TDS, THz-TDP, Mie scattering, Monte Carlo, Tumor budding, degree of polarization (DOP), Diffused scattering.

*M. Hassan Arbab, hassan.arbab@stonybrook.edu

1 Introduction

With rapid advancement of terahertz (THz) spectroscopic methods, this range of electromagnetic frequencies has attracted more attention in the biomedical optics field in recent years.^{1,2} Several biological applications of THz imaging have been explored, including ex vivo experiments on cancer diagnostics,³⁻⁶ and in vivo studies on skin burn classification.⁷⁻⁹ Typically, these studies have explored the dielectric permittivity of the tissue in order to examine sample properties and to differentiate between healthy and diseased specimen. Particularly, most THz in vivo applications

focus on the water content of different tissue types. In comparison, very few studies have used the scattering of the THz light from biological tissue as a diagnostic modality. With an increase in SNR and advancements in THz technology, scattering measurements could play an important role in characterization and classification of some tissue types.

Study of the dielectric permittivity of tissue often assumes a homogeneous structure, or alternatively employs an effective medium theory. This approach can be oversimplifying in many disease conditions. In particular, at the edges of certain types of cancerous tumors such as colon cancer, oral squamous cell carcinoma, and breast cancer, the formation of tumor budding and poorly differentiated clusters can occur, where parts of the tumor break off and form small clusters within otherwise healthy tissue.¹⁰ It has been shown that these features can be independent prognostic factors for lymph node metastasis and patient survival.^{11,12} Current methods for determining the extent of growth of these features include hematoxylin and eosin (H&E) staining and immunohistochemistry.¹³ Other disease conditions can also create a change in the scattering properties of tissue. For example, burns can cause a destruction of higher-scattering features such as hair follicles and sweat glands in the skin.

A promising method for studying these tissue media is through the detection of polarimetric signal contrast in scattered light. Xu and Arbab recently developed a model for Mie scattering of broadband terahertz light in biological media using Monte Carlo methods.¹⁴ Light-scattering models have been used extensively in biophotonics to evaluate the potential for various modalities of optical imaging to detect different forms of skin,¹⁵ gastric,¹⁶ breast,^{17,18} prostate¹⁹ and cervical cancer²⁰ subtypes, and to investigate contrast mechanisms and sensitivity to tissue changes with disease.²¹ Also, polarized scattering light spectroscopy has been investigated for use in endoscopic and laparoscopic imaging of various cancers, including colonic polyps²² and peritoneal lesions.²³

Similarly, polarization measurements of the reflected THz light have been explored for delineation between cancerous and healthy tissue;^{24,25} however, the mechanisms behind the polarization response differences between the types of tissue are yet to be studied in THz frequencies. Given the recent development of various THz ellipsometry and polarimetry systems,²⁶⁻³¹ there is a timely need for computational models that can explain the observed phenomena.

In this paper, we present Monte Carlo simulation and experimental phantom as well as ex vivo measurements of polarization changes due to Mie scattering from structures within tissue, indicating different degrees of disease progression. We explore the potential utility of diffuse scattering measurements for the THz polarimetric diagnosis of disease processes and other THz biophotonics applications.

2 Methods

2.1 Terahertz diffused scattering spectral measurement

Broadband terahertz time-domain spectroscopic (THz-TDS) measurements were performed using the experimental setup shown in Fig. 1(a). In the emission arm, a photoconductive antenna (PCA) was excited using a 1560 nm femtosecond laser, which was then focused onto the sample using a pair of collimating and focusing lenses (L1). In the detection arm, which had the ability to rotate from 0-160 degrees, the light passes through a wire-grid polarizer (WGP) between the collimating (L2) and focusing lenses (L1) before it reached the PCA detector. To quantify the diffused component of the THz scattered light, we used a sample composed of 180-micron polyethylene scattering particles within a polyethylene container with a volume density of 0.3 g/cm³ (Fig. 1(b)). We obtained THz-TDS scattering measurements at 10-degree intervals from 0-160 degrees. Separately, we captured a 180-degree scattering measurement by placing a beam splitter in the emission path,

and scaling the measurement according to the loss of power through the beam splitter. For each angle, scattering measurements were collected at 36 locations on the sample container, each 5 mm apart, with 100 time-domain trace averages to separate the coherent and incoherent components of the signal. Figure 1(c) shows the phantom sample that will be used in the later experiments. Figure 1(d-e) shows the angular distribution of the detected coherent and incoherent power, respectively, from 0.2 to 1.4 THz, normalized by the peak value of the coherent power. We observed a sharp decrease in coherent power from 0-20 degrees, with an increase past 160 degrees. In contrast, the incoherent power remained above our system's detectable threshold (greater than -60dB) at all angles except 70-120 degrees. These results show that diffusely back-scattered beam at about 140 degrees is dominated by the incoherent scattered photons that can carry the information regarding tissue structures. Due to this sharp contrast between the incoherent and coherent power in the diffuse backscattering direction, we chose to obtain the subsequent phantom measurements at 140 degrees. These scattering data were measured by raster scanning the phantom sample over the beam focus, moving a distance of 2mm for each pixel, for x and y-polarization measurements. Two raster scans were performed for each sample, with the polarization state of the wire-grid polarizer and THz detector rotated between each scan. A total of 100 measurements were recorded for each polarization state over a 2 cm by 2 cm area.

2.2 Fabrication of tissue phantoms with scattering particles

Our objective is to emulate a tissue sample, in which spherical structures having a lower refractive index and absorption coefficient than the medium are embedded. Examples of such structures include hair follicles, empty sweat glands, or certain cancer types such as oral squamous cell carcinoma.^{32,33} We constructed such phantoms using polypropylene particles embedded in gelatin.

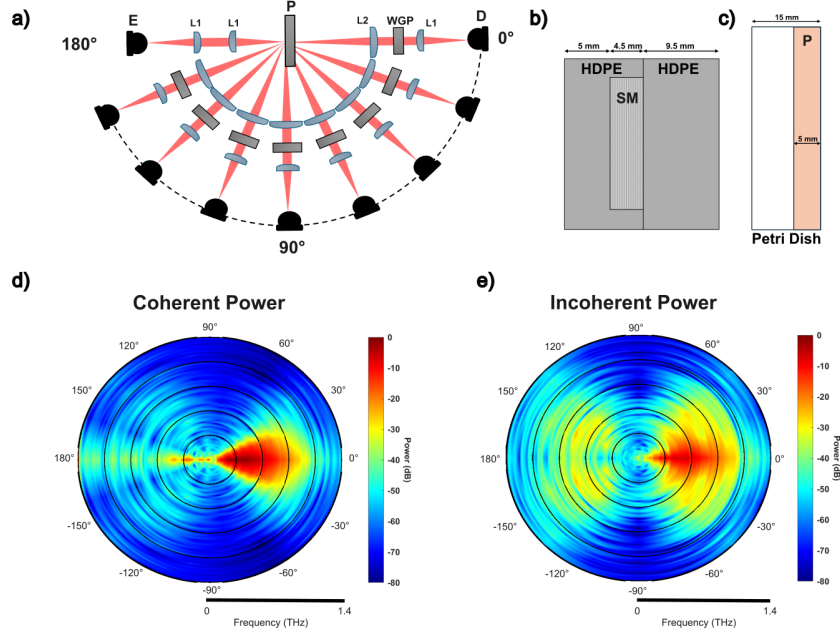


Fig 1 (a) Diagram of the experimental setup. E = Emitter, D = Detector, L1 = TPX lens with 50 mm focal length, L2 = PTFE lens with 100 mm focal length, WGP = Wire-Grid Polarizer, and P = Phantom. (b) HDPE container used for holding scattering material (SM). (c) Phantom design within petri dish. (d-e) Angular distribution of coherent and incoherent power measured from LDPE scattering material. Measurement from 160-180 degrees were made with the addition of a beam-splitter in the beam path.

A 15% bovine skin gelatin solution (Sigma Aldrich, Inc.) was heated to 40° C. Once the desired temperature was reached, polypropylene particles (MicroPowders, Inc.) were rapidly mixed into the solution. The solution was then poured into a Petri dish to a height of about 5mm. Due to the rapid viscosity change as the gelatin cools, the particles remained suspended within the gelatin and did not settle. This process was repeated for 4 phantoms, with differing particle sizes and concentrations. However, due to clumping of the particles during the mixing process, causing the phantoms to differ from the intended parameters, the size and concentrations of the particles were later analyzed using optical microscopy and ImageJ software.³⁴

Particle sizes for the phantoms were chosen based on the wavelengths of THz light and the size of relevant tissue structures, such as tumor buds and hair follicles. Figure 2(a) shows a diagram of the sizes of relevant tissue structures compared to the THz wavelengths. To ensure the resultant

electromagnetic scattering is within the Mie regime, we calculated the size parameter $x=2\pi r/\lambda$ where r is the radius of the particles, n is the refractive index of the host medium (assumed to be the refractive index of skin), and λ is the wavelength for relevant particle sizes. As shown in Fig. 2(b), all relevant particle sizes fall within a size parameter between 0.2-20 within our system's usable bandwidth of 0.2-1.5 THz, indicating that the primary scattering will be due to Mie theory. Particle sizes for the phantoms were chosen based on the sizes of sweat glands and poorly differentiated tumor clusters to be reasonably detected with our experimental setup. Figure 2(c) shows examples of three of our phantoms, with varying particle sizes.

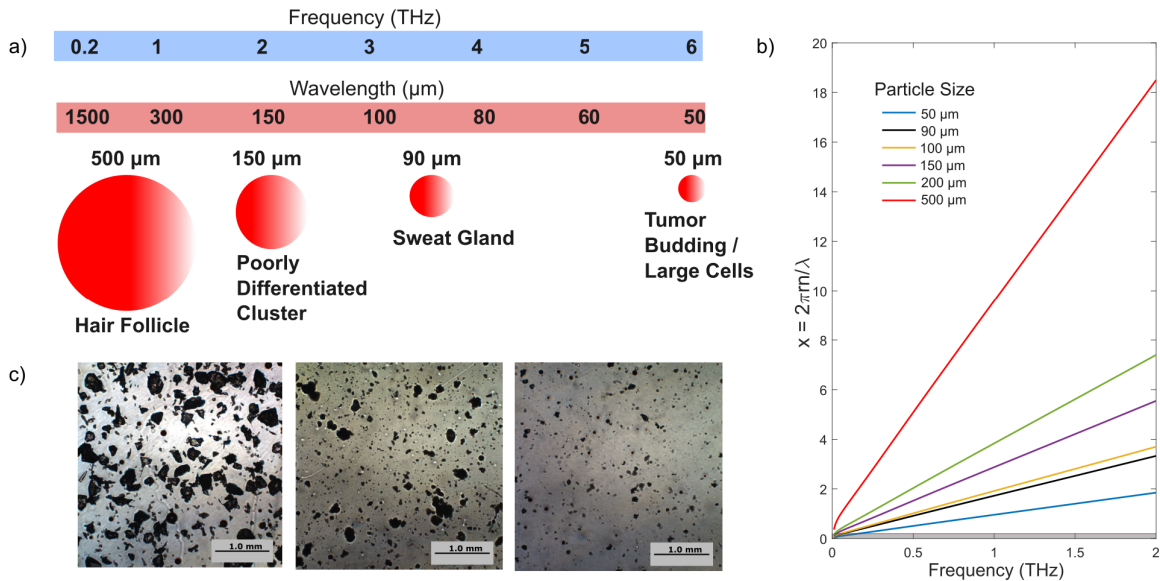


Fig 2 a) Artistic representation of relevant spherical tissue structure sizes compared to Terahertz wavelengths.³⁵ b) Mie scattering parameter for particle sizes 50-500 μm . c) Representative optical microscopy images of fabricated phantoms.

We measured the dielectric properties of the gelatin and polypropylene particles for use in our Monte Carlo model. In the case of the polypropylene particles, we took transmission measurements at the 0-degree angle of our setup through a pellet constructed by pressing the polypropylene particles under a 3000 psi load for approximately 1 hour. For the gelatin medium, the recently

developed PHASR scanner^{28,36} was used to obtain reflection measurements at normal incidence angle on a pure 15% gelatin sample. The calculated index of refraction and absorption coefficients were averaged across 100 pixels for both the particles and gelatin, shown in Fig. 3. The measured refractive index of the polypropylene particles is slightly lower than the expected value of ~ 1.51 in the THz frequency range;^{37,38} however, this could be due to manufacturing variability or remaining air pockets within the pressed pellet sample. The measured absorption coefficient had a value of $< 2 \text{ cm}^{-1}$ for the entire bandwidth of our system. The measured refractive index and absorption coefficient of gelatin were higher than those of skin, but below those of water.

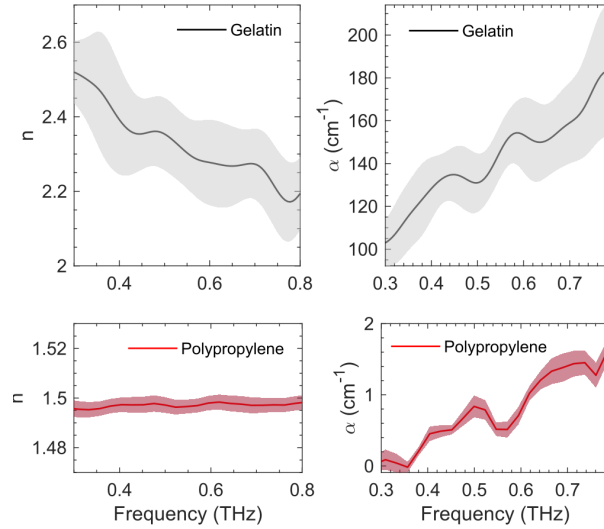


Fig 3 Measured refractive indexes and absorption coefficients of gelatin and polypropylene.

2.3 Monte Carlo simulations

The multi-layer diffused reflectance and polarization Monte Carlo code used for modeling the samples was developed by Xu and Arbab,¹⁴ based on the Meridian Plane Polarized Light Monte Carlo Code by Ramella-Roman et al.,³⁹ with alterations to the Mie scattering parameters to account for an absorbing host medium. Figure 4 describes the flowchart of the altered Polarized Light Monte

Carlo code with the addition of a Mie Calculator to generate the input parameters. The Mie Calculator takes an input of the dielectric properties of the medium and particles, the size of the particles, and the number density of the particles and produces the asymmetric factor g (the average cosine of the scattering angle) and the scattering and absorption coefficients μ_s and μ_a , given by⁴⁰

$$\mu_s = \frac{2\pi\rho}{|n_m|^2 k_0^2} \sum_{j=1}^{\infty} (2j+1)(|a_j|^2 + |b_j|^2) \quad (1)$$

$$\mu_a = \frac{2\pi\rho}{\Re(n_m)k_0^2} \Im\left[\left(\sum_{j=1}^{\infty} (2j+1)(|c_j|^2 \psi_j(z)\psi_j'^*(z) - |d_j|^2 \psi_j'(z)\psi_j^*(z))\right)/n_p\right] \quad (2)$$

where n_m and n_p are the complex refractive indexes of the medium and particles respectively, $k_0 = 2\pi/\lambda$ is the wave vector, ρ is the number density of the particles a_j , b_j , c_j , and d_j are the Mie coefficients, and $\psi_j(z)$ is a Ricatti-Bessel function where $z = n_p k_0 r$. In addition to these parameters, the Mie Calculator also produces the scattering matrix that represents the relationship between the incident (E_i) and scattered (E_s) field amplitudes using Jones calculus:

$$\begin{bmatrix} E_s^\perp \\ E_s^\parallel \end{bmatrix} \propto \begin{bmatrix} S_1 & 0 \\ 0 & S_2 \end{bmatrix} \begin{bmatrix} E_i^\perp \\ E_i^\parallel \end{bmatrix}. \quad (3)$$

The Mueller calculus transform of Equation 3 is given by

$$\begin{bmatrix} I_s \\ Q_s \\ U_s \\ V_s \end{bmatrix} \propto \begin{bmatrix} S_{11} & S_{12} & 0 & 0 \\ S_{12} & S_{11} & 0 & 0 \\ 0 & 0 & S_{33} & S_{34} \\ 0 & 0 & -S_{34} & S_{33} \end{bmatrix} \begin{bmatrix} I_i \\ Q_i \\ U_i \\ V_i \end{bmatrix}, \quad (4)$$

where I, Q, U, and V are the Stokes parameters of the incident and scattered light. The Polarized Light Monte Carlo code produces the spatial Stokes Parameters for a given set of outputs from the Mie Calculator and an initial incident light polarization. Using four different incident light polarizations (specifically horizontal linearly polarized, vertical linearly polarized, 45° linearly polarized, and right circularly polarized) the spatial Mueller Matrix parameters can be calculated. Additionally, using spatially averaged Stokes parameters from a linearly polarized incident light, the degree of polarization (DOP) of the scattered beam can be calculated as,

$$DOP = \frac{\sqrt{Q^2 + U^2 + V^2}}{I}. \quad (5)$$

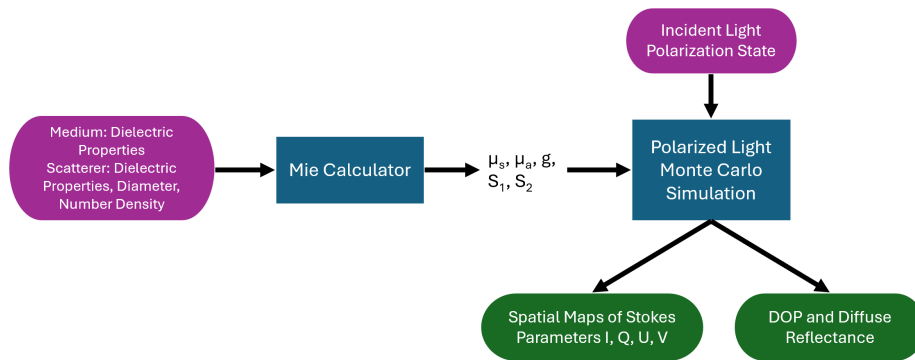


Fig 4 Flowchart indicating the simulation input parameters and the interface between the Mie Calculator and Polarized Light Monte Carlo model.

3 Results

3.1 Evaluation of average particle size and density in phantoms

Particle sizes and concentrations for each phantom were evaluated using optical microscopy and an ImageJ workflow. A threshold was set in ImageJ to discard any detected particles below a diameter of 75μm, to eliminate any image artifacts and small particles that were unlikely to contribute to

the signal. Twenty-five microscope images such as those in Fig. 2(c) were taken of each phantom, and 10 ROIs of 1mm x 1mm field of view were delineated for each image, giving a total of 250 measurements of average particle size and concentration for each phantom. These measurements were averaged to give an average particle size and concentration for each phantom as inputs for the simulation. The concentration calculated using this procedure provides the surface density in units of particles/mm². To convert this quantity to volume density, it was divided by the summation of the depth of field of the microscope and twice the particle diameter size. Due to inhomogeneities within the phantoms, such as clumping of the particles, some phantoms produces inconsistent density and particle size numbers and were therefore excluded from further analysis. Table 1 summarizes the average particle sizes and volume density for the final four phantoms as input parameters for Monte Carlo analysis in the following section.

Table 1 Average particle size and volume density of the phantoms

Phantom	Particle Diameter (μm)	Surface Density (particles/mm ²)	Volume Density (mm ⁻³)
A	115	3	10
B	130	2	7
C	180	3.5	8.5
D	280	6.5	10.5

3.2 Monte Carlo simulation results

Using the refractive indices calculated in Section 2.3 and the particle sizes and volume densities determined in Section 3.1, the Polarized Light Monte Carlo model was used to simulated the THz polarimetric response of the final four phantoms. For each particle size, we calculated the asymmetric factor and the scattering efficiency, which is the ratio of the scattering cross-section to the geometric area of a particle. Figure 5 shows the calculated scattering efficiency and asymmetric

factor for each particle size. As the particle size increases, the scattering efficiency and asymmetric factor both increase in the lower frequencies up to about 1 THz.

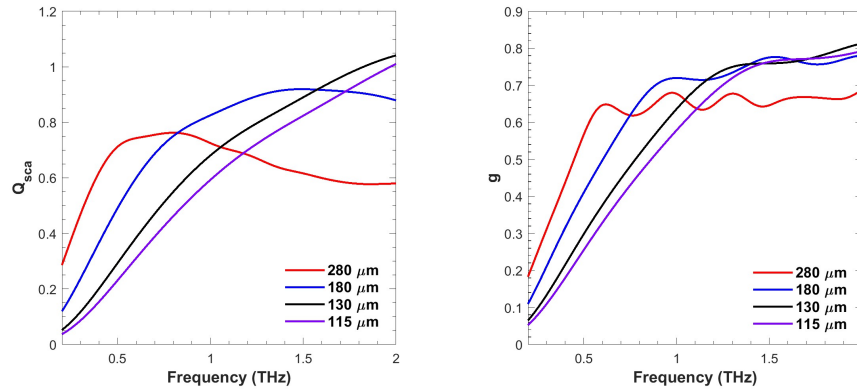


Fig 5 Calculated scattering efficiency and asymmetric factor for relevant particle sizes.

To calculator the Mueller Matrix of each sample, spatial Stokes vector maps were generated for each phantom for incident light polarizations of parallel, perpendicular, and 45° linearly polarized, and right circularly polarized. Figure 6 presents a comparison between the Stokes parameters maps of Phantoms A and D, having the smallest and largest particle sizes respectively, when illuminated with a 45° linearly polarized incident THz beam. The spatial maps reveal the greater intensity of scattered light received with the simulation of Phantom D compared to Phantom A, matching the expectations of a higher reflectance with a larger particle size. Using the spatial maps from all four incident light polarizations, the spatial Mueller matrix maps, shown in Fig. 7, were calculated. The simulated Mueller matrices for Phantoms D and A show similar angular distribution patterns, with the patterns being much less resolved with Phantom A, similar to the Stokes parameter maps. The clearest difference between the two maps is present in element M_{22} where the values of the angular distribution pattern of Phantom D are closer to zero than the values of Phantom A. This difference is also reflected in element M_{33} where the values of Phantom A are much closer to -1

than Phantom D. To better analyze the differences between the simulated Mueller matrices of the phantoms, we calculated the pixel sum of each of the Mueller matrix element maps to obtain a singular Mueller matrix for each phantom. The Mueller matrices of phantoms A and D, i.e., M_A and M_D , are given below.

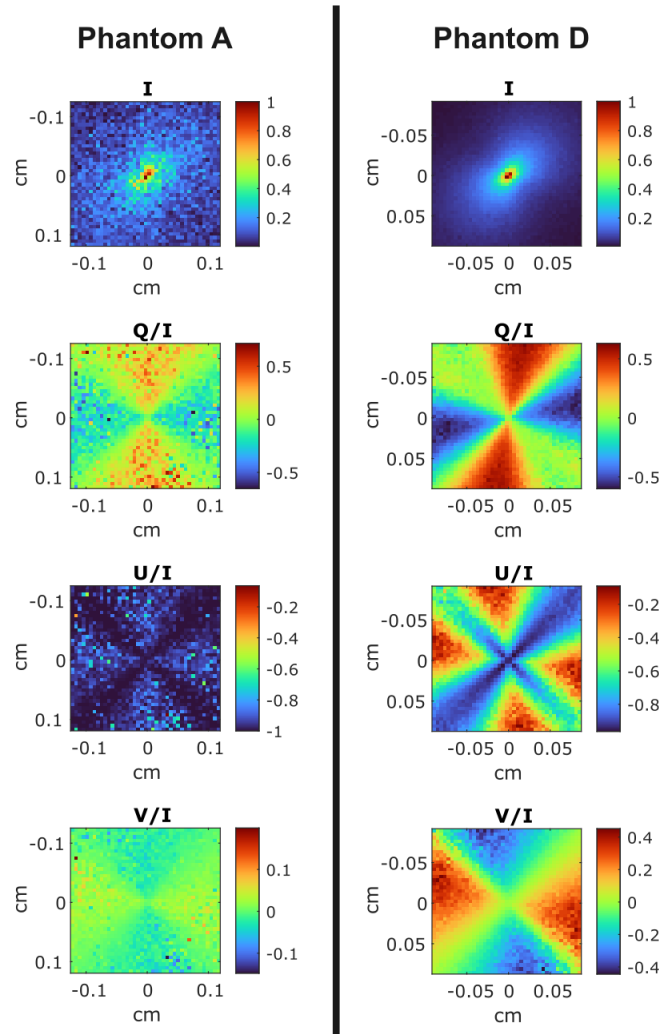


Fig 6 Spatial map of the simulated Stokes vector, IQUV, for Phantoms A and D.

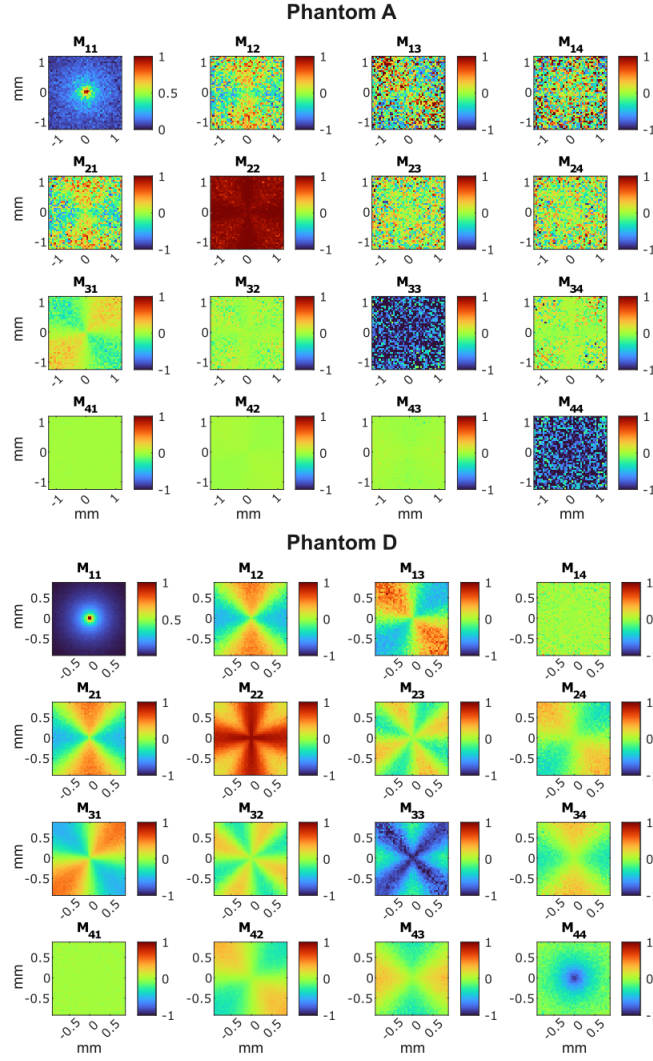


Fig 7 Simulated Mueller Matrix for Phantoms A and D

$$M_A = 3.05 \times 10^{-4} \begin{bmatrix} 1.000 & -0.003 & 0.008 & 0.008 \\ -0.003 & 0.922 & 0.004 & 0.004 \\ -0.002 & -0.001 & -0.926 & 0.000 \\ 0.000 & 0.000 & 0.000 & -0.850 \end{bmatrix} \quad (6)$$

$$M_D = 4.23 \times 10^{-3} \begin{bmatrix} 1.000 & 0.000 & -0.001 & -0.001 \\ 0.000 & 0.586 & 0.000 & 0.000 \\ 0.000 & 0.000 & -0.586 & -0.001 \\ 0.000 & 0.000 & 0.000 & -0.207 \end{bmatrix} \quad (7)$$

These matrices can be decomposed using Lu and Chipman decomposition⁴¹ as:

$$M_{\Delta,A} \approx \begin{bmatrix} 1 & 0 & 0 & 0 \\ 0 & 0.921 & 0 & 0 \\ 0 & 0 & 0.925 & 0 \\ 0 & 0 & 0 & 0.849 \end{bmatrix}, M_{R,A} \approx \begin{bmatrix} 1 & 0 & 0 & 0 \\ 0 & 1 & 0 & 0 \\ 0 & 0 & -1 & 0 \\ 0 & 0 & 0 & -1 \end{bmatrix}, M_{D,A} \approx 3.050 \times 10^{-4} \mathbf{I} \quad (8)$$

$$M_{\Delta,D} \approx \begin{bmatrix} 1 & 0 & 0 & 0 \\ 0 & 0.586 & 0 & 0 \\ 0 & 0 & 0.586 & 0 \\ 0 & 0 & 0 & 0.207 \end{bmatrix}, M_{R,D} \approx \begin{bmatrix} 1 & 0 & 0 & 0 \\ 0 & 1 & 0 & 0 \\ 0 & 0 & -1 & 0 \\ 0 & 0 & 0 & -1 \end{bmatrix}, M_{D,D} \approx 4.230 \times 10^{-3} \mathbf{I} \quad (9)$$

Each of the phantom's Mueller matrices can be decomposed as approximately a uniform attenuator and nonuniform depolarizer. Since this simulation records the reflected photons instead of transmitted photons through the medium, the diagonal value of the uniform attenuator matrix represents the diffuse reflectance of the sample. The diagonal depolarizer matrix can be represented with single value: the degree of polarization of linear light "p", where the depolarization matrix is $\text{diag}[1, p, p, 2p-1]$. Since the Mueller matrix and its decomposition can be represented in terms of

only the diffuse reflectance and linear degree of polarization, only these two values are necessary to characterize the polarimetric response of these sample. These two parameters can be obtained by a measurement of either linear or circularly polarized light scattered to a diffuse angle; therefore, measurement of four different initial polarization states as would typically be done for a full Mueller matrix characterization with spherical symmetry is unnecessary in this case, according to this simulation. Using the spatial maps generated from linearly polarized light, we calculated the diffuse reflectance as the Stokes parameter I and the degree of polarization using Equation 5 to compare with experimental results.

3.3 Comparison between model and experimental data

For each phantom, time domain THz-TDS waveforms were converted into the complex fourier domain to produce E_x and E_y spectra. Stokes parameters were calculated using,

$$I = \langle |E_x|^2 \rangle + \langle |E_y|^2 \rangle, Q = \langle |E_x|^2 \rangle - \langle |E_y|^2 \rangle, U = 2\Re\langle E_x E_y^* \rangle, V = -2i\Im\langle E_x E_y^* \rangle. \quad (10)$$

The intensity was taken as stokes parameter I averaged over 100 pixels, while the degree of polarization (DOP) was calculated using Equation 5 with the stoke parameters averaged across 100 pixels with E_x and E_y deconvolved with an air reference taken at 0 degrees transmission. The simulated result for the diffuse reflectance was converted into reflected intensity by multiplying the simulation by the spectrum of the air reference. Figure 8 presents the simulated results for linearly polarized light alongside the experimental results for the four phantoms analyzed. The diffuse scattered intensity between 0.2 and 1.2 THz has a similar trend between the simulation and experimental results, show a higher intensity at lower frequencies and an exponential roll-

off with increasing frequency. As the diameter of the particles increases, the scattered intensity becomes greater. The absolute values of the diffuse scattered intensity between the simulation and experiment cannot be directly compared because the simulation results represents photons from all backscattered angles, whereas the experimental data was collected only in a 20° detection cone. The diffused scattered intensity is also very sensitive to slight changes in the alignment of the experimental system.

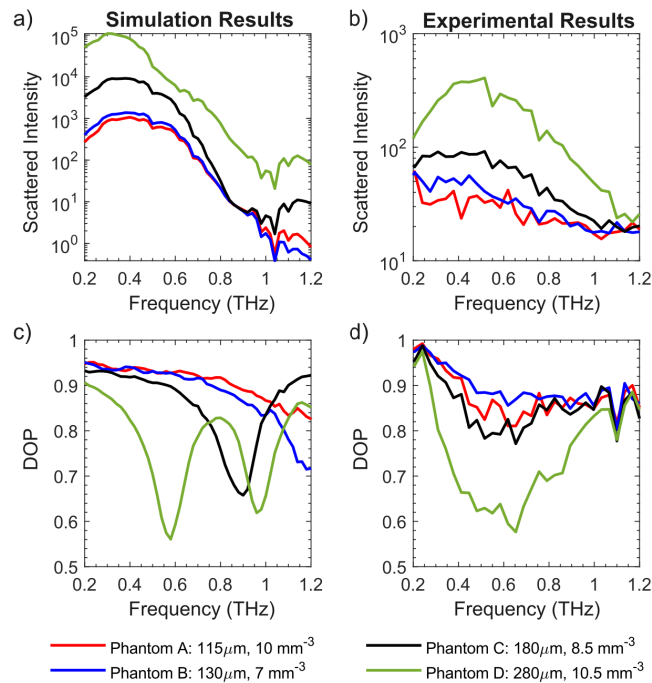


Fig 8 Comparison between simulation and experimental data.

The DOP parameter, which is less susceptible to the miss-alignments in the system, shows a similar trend to the diffuse scattered intensity results. Due to the SNR and bandwidth limitations of our system, DOP measurements past 0.8 THz are not as reliable. As shown in Fig. 8, phantom D shows a similar trend in both simulation and experimental data with a drop in DOP to around 0.6 at roughly 0.6 THz. Phantom C has less of a drop in DOP from 0.2-0.8 THz than Phantom D, but more of a drop than Phantoms A or B. Phantoms A and B have an opposite trend than expected, but

this reveals the limitations of our system. Since the frequency location of the drop in DOP depends on particle size, to measure a drop in DOP from smaller particle sizes, a larger bandwidth than our experimental setup would be required. Despite the lack of agreement with Phantoms A and B, there is still a significant difference in measured DOP results between Phantom D and Phantoms A and B. Additionally, DOP is much less sensitive to the alignment of the setup, so it could be a more reliable diagnostic marker than reflected intensity.

3.4 Experimental Data of A Porcine Skin Burn

To demonstrate the potential of DOP and diffuse backscattered intensity in realistic tissue conditions, we present results of THz measurements of an ex vivo porcine skin burn. A 1-inch full thickness burn was induced by applying a brass bar heated to 180°C to the skin for 5 minutes. We mounted the porcine skin in our setup at 140° and took measurements of a 2 x 3.5 cm area with a 1mm pixel size. Each pixel had 10 measurements taken with 10 time-averages. Using the 10 measurements per pixel, we calculated the intensity as the Stokes parameter I and the DOP using Eqns. 5 and 6. Figure 9 presents spatial maps of the DOP and intensity at 0.6 THz compared with a photograph of the burn area imaged. Both maps show contrast between the burn and healthy tissue. A higher DOP values for the burn could be attributed to the destruction of large skin structures such as hair follicles and sweat glands, overall decreasing the average size of scatterers within the skin. The higher intensity values for the burn could be attributed to decreased absorption from the skin due to water loss from the heating of the skin in the production of the burn.

To compare the frequency-dependent burn measurements with the healthy tissue measurements, four ROIs were averaged and plotted, two burn ROIs and two healthy tissue ROIs, each with 16 pixels. Figure 10 shows these frequency-dependent curves and their locations on the THz

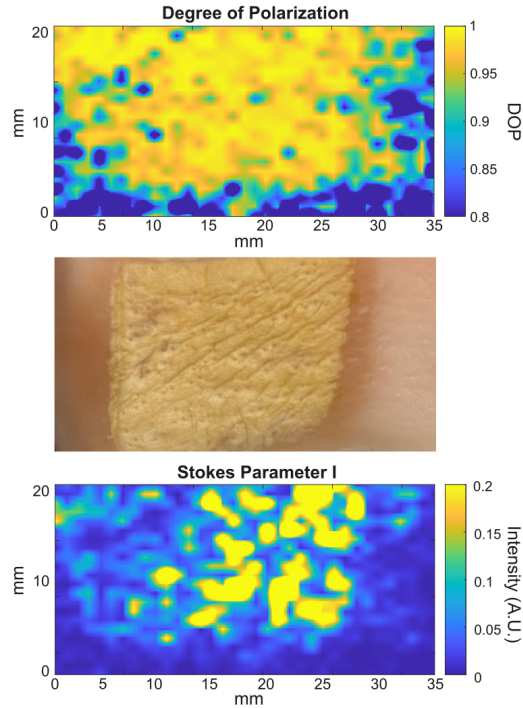


Fig 9 DOP and diffused scattered intensity maps of a porcine skin burn at 0.6 THz.

maps. These curves reveal that the healthy tissue DOP drops much faster than the burn DOP from 0.2-0.8 THz. According to our simulation data, this would indicate a decrease in the size of scatterers within the burn tissue compared to healthy tissue. We also observe a large contrast in the diffuse intensity between the burn and healthy tissue. According to the Mie scattering simulation, an increase in DOP should coincide with a decrease in diffuse intensity, but the opposite pattern is seen with this burn. This could be attributed to a difference in absorption coefficient since there is a decrease in water content of the tissue after a burn injury is inflicted. This would increase the diffuse intensity since the overall albedo would increase.

4 Discussion

Extending the simulation results to a larger bandwidth of 2 THz (Fig. 11) shows more clearly the frequency-dependent features of the DOP. These results reveal that as the particle size increases,

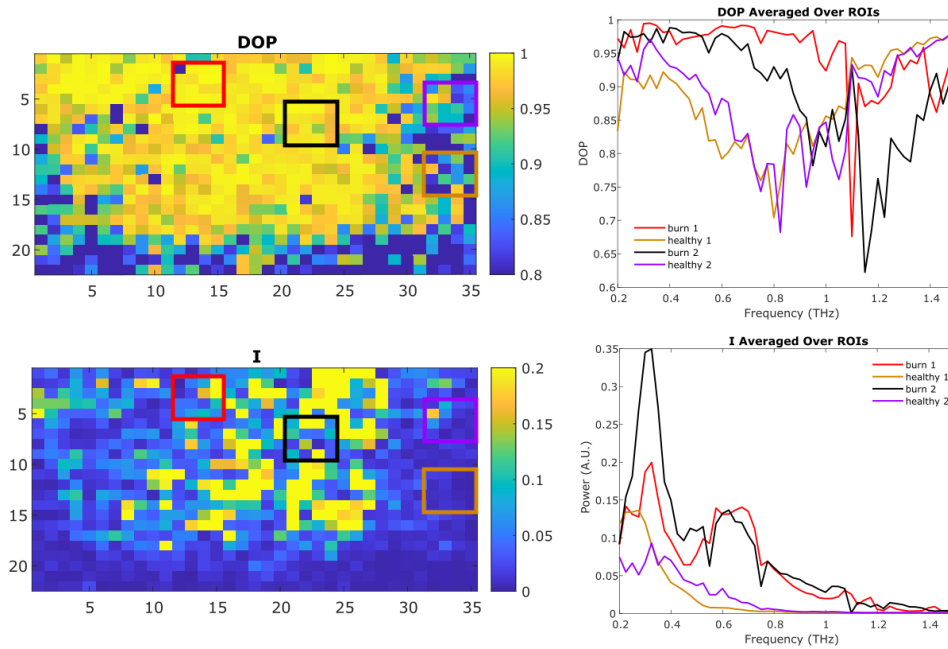


Fig 10 Frequency-dependent DOP and Intensity of two burn ROIs and two healthy porcine skin ROIs. Each ROI is composed of 16 pixels.

the diffuse reflectance increases. Additionally, the spectral location of the first minima in the DOP (for both linearly and circularly polarized light) moves to lower frequencies as the particle size increases. Xu and Arbab showed in their analysis of this simulation method that the depth of the minima in DOP curves is a function of the concentration of the particles. In other word, a larger drop in DOP corresponds to a higher concentration;¹⁴ therefore, spectral dependence of the DOP can allow for determination of both the concentration and size of particles, given a frequency-dependent DOP measurement with sufficient signal-to-noise ratio and bandwidth. The circular DOP (DOP_c) is related to the linear DOP (DOP_l) by the relationship $DOP_c = 2DOP_l - 1$. Finally, the magnitude of the diffuse reflectance changes with both particle size and concentration. Our results suggest that the particle size-dependent pattern in the diffuse reflectance may be difficult to resolve with current THz systems.

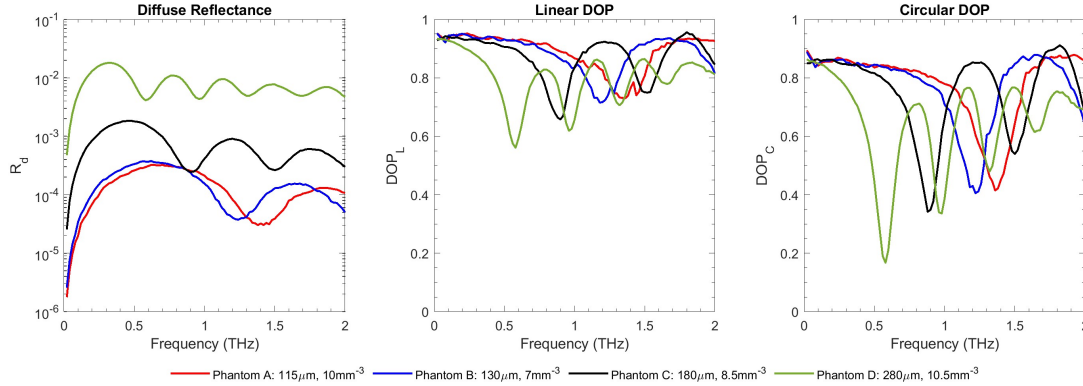


Fig 11 Simulated Diffuse Reflectance and DOP up to 2 THz.

Given the results of our phantom measurements and the diffused polarimetric imaging of a porcine skin burn, contrast can be seen with the DOP and diffuse scattered intensity between different sizes of scattering particles in tissue environments; however, these signal contrasts are best observed when the difference between the sizes of particles are large. Observations of smaller differences in concentration and size of scattering particles are limited by our current bandwidth and SNR. A THz system with a larger bandwidth, such as the one developed by Xu et al. with a bandwidth of 8 THz using electro-optic crystals instead of PCA emitters and detectors,⁴² could aid in resolving these features for smaller particle size differences.

Lastly, in this work we assumed that the surface of the phantom and the ex vivo skin is optically flat and smooth. We have previously studied the depolarization of THz waves in the backscattered speckle fields due to surface roughness of the sample.²⁷ In general, the DOP parameter can be spectrally affected by both surface depolarization as well as scattering by the internal structures of the skin. Several signal processing and experimental measurement techniques can be used to characterize the relative contribution of each source of depolarization. Examples of these methods include wave signal decomposition^{43,44} and statistical speckle analysis.²⁷

5 Conclusion

We have presented simulation and experimental results for Mie scattering of THz light due to structures in biological tissue, such as hair follicles, sweat glands and tumor budding. Simulations revealed the potential for diffuse backscattered intensity and Degree of Polarization (DOP) parameter to distinguish between different scattering scenarios. Simulated Mueller matrices showed that for spherical particles in an absorbing medium, only one polarization measurement from either linearly or circularly polarized light is needed to construct a full Mueller matrix of the sample. Additionally, we decomposed the Mueller matrices of the tissue according to the Lu-Chipman formalism and summarized the key sources of the scattering signal contrast in highly absorptive media. Experimental measurements of phantoms of moderately sized tumor budding and poorly differentiated clusters confirmed the frequency-dependent patterns from our simulation and showed the potential of DOP and diffuse scattered intensity for diagnosis. Finally, experimental measurements of a porcine skin burn showed contrast between burned regions and healthy regions of tissue, demonstrating the ability of this technique to distinguish between disease states in *ex vivo* tissue. Future work in this direction would include extending our phantom measurements to *ex vivo* cancer tissue, increasing the bandwidth of the measurements to better resolve the frequency-dependent features.

References

- 1 A. Leitenstorfer, A. S. Moskalenko, T. Kampfrath, *et al.*, “The 2023 terahertz science and technology roadmap,” *Journal of Physics D: Applied Physics* **56**(22), 223001 (2023).
- 2 X. Chen, H. Lindley-Hatcher, R. I. Stantchev, *et al.*, “Terahertz (THz) biophotonics tech-

- nology: Instrumentation, techniques, and biomedical applications,” *Chem. Phys. Rev.* **3**(1), 011311 (2022).
- 3 P. C. Ashworth, E. Pickwell-MacPherson, E. Provenzano, *et al.*, “Terahertz pulsed spectroscopy of freshly excised human breast cancer,” *Optics Express* **17**, 12444–12454 (2009). Publisher: Optica Publishing Group.
- 4 M. El-Shenawee, N. Vohra, T. Bowman, *et al.*, “Cancer detection in excised breast tumors using terahertz imaging and spectroscopy,” *Biomedical Spectroscopy and Imaging* **8**, 1–9 (2019).
- 5 B. Fan, V. A. Neel, and A. N. Yaroslavsky, “Multimodal imaging for nonmelanoma skin cancer margin delineation,” *Lasers in Surgery and Medicine* **49**(3), 319–326 (2017). eprint: <https://onlinelibrary.wiley.com/doi/pdf/10.1002/lsm.22552>.
- 6 Y. C. Sim, J. Y. Park, K.-M. Ahn, *et al.*, “Terahertz imaging of excised oral cancer at frozen temperature,” *Biomedical Optics Express* **4**, 1413–1421 (2013). Publisher: Optica Publishing Group.
- 7 M. E. Khani, O. B. Osman, Z. B. Harris, *et al.*, “Accurate and early prediction of the wound healing outcome of burn injuries using the wavelet Shannon entropy of terahertz time-domain waveforms,” *Journal of Biomedical Optics* **27**(11), 116001 (2022).
- 8 O. B. Osman, Z. B. Harris, M. E. Khani, *et al.*, “Deep neural network classification of in vivo burn injuries with different etiologies using terahertz time-domain spectral imaging,” *Biomed. Opt. Express* **13**, 1855–1868 (2022). Publisher: Optica Publishing Group.
- 9 M. E. Khani, Z. B. Harris, O. B. Osman, *et al.*, “Triage of in vivo burn injuries and prediction of wound healing outcome using neural networks and modeling of the terahertz permittivity

- based on the double debye dielectric parameters,” *Biomedical Optics Express* **14**, 918–931 (2023).
- 10 A. Lugli, R. Kirsch, Y. Ajioka, *et al.*, “Recommendations for reporting tumor budding in colorectal cancer based on the International Tumor Budding Consensus Conference (ITBCC) 2016,” *Modern Pathology* **30**, 1299–1311 (2017).
 - 11 D. Venkatesh and T. Smitha, “Cell budding,” *Journal of Oral and Maxillofacial Pathology : JOMFP* **23**(3), 330–332 (2019).
 - 12 L. Reggiani Bonetti, V. Barresi, S. Bettelli, *et al.*, “Poorly differentiated clusters (PDC) in colorectal cancer: what is and ought to be known,” *Diagnostic Pathology* **11**, 31 (2016).
 - 13 A. Lugli, I. Zlobec, M. D. Berger, *et al.*, “Tumour budding in solid cancers,” *Nature Reviews Clinical Oncology* **18**(2), 101–115 (2021).
 - 14 K. Xu and M. H. Arbab, “Terahertz polarimetric imaging of biological tissue: Monte carlo modeling of signal contrast mechanisms due to mie scattering,” *Biomed. Opt. Express* **15**, 2328–2342 (2024).
 - 15 A. Garcia-Uribe, J. Zou, M. Duvic, *et al.*, “In vivo diagnosis of melanoma and nonmelanoma skin cancer using oblique incidence diffuse reflectance spectrometry,” *Cancer Research* **72**(11), 2738–2745 (2012).
 - 16 N. Nishizawa and T. Kuchimaru, “Depth estimation of tumor invasion in early gastric cancer using scattering of circularly polarized light: Monte Carlo Simulation study,” *Journal of Biophotonics* **15**(10), e202200062 (2022).
_eprint: <https://onlinelibrary.wiley.com/doi/pdf/10.1002/jbio.202200062>.
 - 17 M. L. Altoe, K. Kalinsky, A. Marone, *et al.*, “Changes in diffuse optical tomography images

- during early stages of neoadjuvant chemotherapy correlate with tumor response in different breast cancer subtypes,” *Clinical Cancer Research* **27**(7), 1949–1957 (2021).
- 18 M. D. Keller, S. K. Majumder, M. C. Kelley, *et al.*, “Autofluorescence and diffuse reflectance spectroscopy and spectral imaging for breast surgical margin analysis,” *Lasers in Surgery and Medicine* **42**(1), 15–23 (2010).
- 19 O. M. A’Amar, L. Liou, E. Rodriguez-Diaz, *et al.*, “Comparison of elastic scattering spectroscopy with histology in ex vivo prostate glands: potential application for optically guided biopsy and directed treatment,” *Lasers in Medical Science* **28**(5), 1323–1329 (2013).
- 20 D. Arifler, C. MacAulay, M. Follen, *et al.*, “Spatially resolved reflectance spectroscopy for diagnosis of cervical precancer: Monte carlo modeling and comparison to clinical measurements,” *Journal of Biomedical Optics* **11**(6), 064027 (2006).
- 21 Z. A. Steelman, D. S. Ho, K. K. Chu, *et al.*, “Light-scattering methods for tissue diagnosis,” *Optica* **6**(4), 479–489 (2019).
- 22 E. Rodriguez-Diaz, Q. Huang, S. R. Cerda, *et al.*, “Endoscopic histological assessment of colonic polyps by using elastic scattering spectroscopy,” *Gastrointestinal Endoscopy* **81**(3), 539–547 (2015). doi: 10.1016/j.gie.2014.07.012.
- 23 R. M. Trout, E. Gnanatheepam, A. Gado, *et al.*, “Polarization enhanced laparoscope for improved visualization of tissue structural changes associated with peritoneal cancer metastasis,” *Biomedical Optics Express* **13**, 571 (2022).
- 24 P. Doradla, K. Alavi, C. S. Joseph, *et al.*, “Detection of colon cancer by continuous-wave terahertz polarization imaging technique,” *Journal of Biomedical Optics* **18**, 090504 (2013).
Publisher: SPIE.

- 25 N. Gurjar, K. Bailey, and M. O. El-Shenawee, “Polarimetry terahertz imaging of human breast cancer surgical specimens,” *Journal of Medical Imaging* **11**, 065503 (2024). Publisher: SPIE.
- 26 X. Chen, E. P. J. Parrott, Z. Huang, *et al.*, “Robust and accurate terahertz time-domain spectroscopic ellipsometry,” *Photon. Res.* **6**, 768–775 (2018).
- 27 K. Xu, Z. B. Harris, and M. H. Arbab, “Polarimetric imaging of back-scattered terahertz speckle fields using a portable scanner,” *Opt. Express* **31**, 11308–11319 (2023).
- 28 Z. B. Harris, K. Xu, and M. H. Arbab, “A handheld polarimetric imaging device and calibration technique for accurate mapping of terahertz stokes vectors,” *Scientific Reports* **14**(1), 17714 (2024).
- 29 E. Castro-Camus, J. Lloyd-Hughes, M. Johnston, *et al.*, “Polarization-sensitive terahertz detection by multicontact photoconductive receivers,” *Applied Physics Letters* **86**(25) (2005).
- 30 C. M. Morris, R. V. Aguilar, A. V. Stier, *et al.*, “Polarization modulation time-domain terahertz polarimetry,” *Optics express* **20**(11), 12303–12317 (2012).
- 31 D. S. Bulgarevich, M. Watanabe, M. Shiwa, *et al.*, “A polarization-sensitive 4-contact detector for terahertz time-domain spectroscopy,” *Optics express* **22**(9), 10332–10340 (2014).
- 32 S. Nourinovin, M. M. Rahman, M. P. Philpott, *et al.*, “Terahertz characterization of ordinary and aggressive types of oral squamous cell carcinoma as a function of cancer stage and treatment efficiency,” *IEEE Transactions on Instrumentation and Measurement* **72**, 1–9 (2023).
- 33 Y. B. Ji, J. M. Kim, Y. H. Lee, *et al.*, “Investigation of keratinizing squamous cell carcinoma of the tongue using terahertz reflection imaging,” *Journal of Infrared, Millimeter, and Terahertz Waves* **40**(2), 247–256 (2019).

- 34 C. A. Schneider, W. S. Rasband, and K. W. Eliceiri, “Nih image to imagej: 25 years of image analysis,” *Nature Methods* **9**(7), 671–675 (2012).
- 35 M. Boxberg, M. Jesinghaus, C. Dorfner, *et al.*, “Tumour budding activity and cell nest size determine patient outcome in oral squamous cell carcinoma: proposal for an adjusted grading system,” *Histopathology* **70**(7), 1125–1137 (2017).
- 36 Z. B. Harris and M. H. Arbab, “Terahertz phasr scanner with 2 khz, 100 ps time-domain trace acquisition rate and an extended field-of-view based on a heliostat design,” *IEEE Transactions on Terahertz Science and Technology* **12**, 619–632 (2022).
- 37 T. Chang, X. Zhang, Q. Guo, *et al.*, “Terahertz Dielectric Spectroscopy Based Thermal Aging Analysis of Polypropylene,” *IEEE Transactions on Terahertz Science and Technology* **10**, 363–369 (2020). Conference Name: IEEE Transactions on Terahertz Science and Technology.
- 38 Y.-S. Jin, G.-J. Kim, and S.-G. Jeon, “Terahertz Dielectric Properties of Polymers,” *Journal of the Korean Physical Society* **49**, 513–517 (2006).
- 39 J. C. Ramella-Roman, S. A. Prahl, and S. L. Jacques, “Three Monte Carlo programs of polarized light transport into scattering media: part I,” *Optics Express* **13**, 4420–4438 (2005). Publisher: Optica Publishing Group.
- 40 P. Yang, B.-C. Gao, W. J. Wiscombe, *et al.*, “Inherent and apparent scattering properties of coated or uncoated spheres embedded in an absorbing host medium,” *Applied Optics* **41**, 2740–2759 (2002). Publisher: Optica Publishing Group.
- 41 S.-Y. Lu and R. A. Chipman, “Interpretation of Mueller matrices based on polar decomposition,” *JOSA A* **13**, 1106–1113 (1996). Publisher: Optica Publishing Group.

- 42 K. Xu, M. Liu, and M. H. Arbab, "Broadband terahertz time-domain polarimetry based on air plasma filament emissions and spinning electro-optic sampling in GaP," *Applied Physics Letters* **120**, 181107 (2022).
- 43 M. Ebrahimkhani and M. H. Arbab, "Extraction of thz absorption signatures obscured by rough surface scattering using discrete wavelet transform," in *2018 43rd International Conference on Infrared, Millimeter, and Terahertz Waves (IRMMW-THz)*, 1–2 (2018).
- 44 M. E. Khani and M. H. Arbab, "Translation-invariant zero-phase wavelet methods for feature extraction in terahertz time-domain spectroscopy," *Sensors* **22**(6) (2022).

List of Figures

- 1 (a) Diagram of the experimental setup. E = Emitter, D = Detector, L1 = TPX lens with 50 mm focal length, L2 = PTFE lens with 100 mm focal length, WGP = Wire-Grid Polarizer, and P = Phantom. (b) HDPE container used for holding scattering material (SM). (c) Phantom design within petri dish. (d-e) Angular distribution of coherent and incoherent power measured from LDPE scattering material. Measurement from 160-180 degrees were made with the addition of a beam-splitter in the beam path.
- 2 a) Artistic representation of relevant spherical tissue structure sizes compared to Terahertz wavelengths.³⁵ b) Mie scattering parameter for particle sizes 50-500 μm . c) Representative optical microscopy images of fabricated phantoms.
- 3 Measured refractive indexes and absorption coefficients of gelatin and polypropylene.

- 4 Flowchart indicating the simulation input parameters and the interface between the Mie Calculator and Polarized Light Monte Carlo model.
- 5 Calculated scattering efficiency and asymmetric factor for relevant particle sizes.
- 6 Spatial map of the simulated Stokes vector, IQUV, for Phantoms A and D.
- 7 Simulated Mueller Matrix for Phantoms A and D
- 8 Comparison between simulation and experimental data.
- 9 DOP and diffused scattered intensity maps of a porcine skin burn at 0.6 THz.
- 10 Frequency-dependent DOP and Intensity of two burn ROIs and two healthy porcine skin ROIs. Each ROI is composed of 16 pixels.
- 11 Simulated Diffuse Reflectance and DOP up to 2 THz.

List of Tables

- 1 Average particle size and volume density of the phantoms